Materials & Design 235 (2023) 112443

Contents lists available at ScienceDirect

Materials & Design

journal homepage: www.elsevier.com/locate/matdes

A first-principles and CALPHAD-assisted phase-field model for microstructure evolution: Application to Mo-V binary alloy systems

Abhishek Kumar Thakur [a,*], Sasa Kovacevic [b,*], Venkateswara Rao Manga [a,c], Pierre A. Deymier [a], Krishna Muralidharan [a,c]

[a] Department of Materials Science and Engineering, University of Arizona, Tucson, AZ 85721, USA
[b] Department of Civil and Environmental Engineering, Imperial College London, London SW7 2AZ, UK
[c] Lunar and Planetary Laboratory, University of Arizona, Tucson, AZ 85721, USA

ARTICLE INFO

Keywords:
Multiscale modeling
Special quasi-random structures
Interfacial energy
Inhomogeneous elasticity
Preferential alloy decomposition

ABSTRACT

A multiscale computational framework combining the first-principles calculations and the CALPHAD approach with the phase-field method is presented to simulate the microstructure evolution in multicomponent steel alloys. We demonstrate the potential of the framework by predicting the microstructural evolution in elastically periodic arrays of the Mo-V binary sub-system. The framework utilizes the first-principles calculations using special quasi-random structures. Hitherto unavailable thermodynamic and material properties of the alloy are obtained by employing the first-principles calculations and the CALPHAD approach and fed into the phase-field model to predict the microstructure evolution at different temperatures within the miscibility gap region. In addition to the temperature and cooling rates, the model incorporates the role of mechanical fields in decomposition kinetics in the Mo-V binary alloy system. Regimes for temperatures and cooling rates at which spinodal decomposition occurs are identified. Applying external loading leads to directional phase separation in the Mo-V binary system. The elastic inhomogeneity in terms of material properties between the two phases initiates the directional alignment while eigenstrains and applied external loading control the degree of alignment. The framework developed is general and extendable to higher multicomponent sub-systems in steel alloys.

1. Introduction

Molybdenum (Mo) and Vanadium (V) are irreplaceable alloying agents in tailoring material properties and micromechanical behavior of multicomponent steel alloys, such as dual-phase steels [1], high entropy alloys [2], and ultrahigh-strength steels [3]. These alloys are widely used in numerous industries, extending from metallurgy, petroleum, oil and gas, mining, and automotive industries to manufacturing various engineering and aerospace components capable of withstanding large temperature ranges and highly corrosive environments [4,5]. The formation of new phases due to the segregation of alloying elements alters the underlying microstructure and considerably influences the performance of these alloys [6]. In this context, characterizing the Mo-V binary sub-system can enable a more comprehensive understanding of their roles in the microstructure evolution and the structure–property-processing interplay in multicomponent steel alloys. Delivering new scientific insights on the Mo-V binary sub-system is indispensable for tailoring enhanced steel alloys for technologically practical applications. To this end, we use a multiscale computational framework to study the microstructure evolution in the Mo-V binary system under various processing and service conditions.

Although the thermodynamic characteristics of the Mo-V binary system, such as the solidus and liquidus boundaries [7], partial molar Gibbs energy and binary interaction parameters [8–10], have been determined, the presence of the miscibility gap for temperatures below 1124.15 K has been recently experimentally confirmed [11]. In experiments [11], Mo-V alloy samples were isothermally heated to a hold temperature of 873.15 K and 1023.15 K and held at those temperatures for seventy days. After the isothermal treatment process, the experiments have shown that the Mo-V solid solution phase has separated into two BCC phases, Mo-rich and V-rich phases (hereafter α and β phases), Fig. 1. The spinodal decomposition and nucleation-growth have been identified as two possible phase decomposition mechanisms [11].

During manufacturing and service life, multicomponent steel alloys are exposed to different temperatures, temperature fluctuations during cooling or heating, and mechanical loading. In addition to these

* Corresponding authors.
E-mail addresses: abhishekkt@arizona.edu (A. Kumar Thakur), s.kovacevic@imperial.ac.uk (S. Kovacevic).

https://doi.org/10.1016/j.matdes.2023.112443
Received 13 August 2023; Received in revised form 26 October 2023; Accepted 29 October 2023
Available online 2 November 2023

environmental conditions, additional mechanical fields arise due to the lattice mismatch between coexisting phases and the difference in material properties due to inhomogeneous composition. Studies have shown that the temperature in terms of cooling rates (CRs) [12] and the presence of stress fields [13] have a significant effect on the temporal evolution and resulting microstructure morphology in solid-state phase transformations. They can entirely suppress or alter the onset of phase separation. Furthermore, the elastic properties and the elastic inhomogeneity of the material play an important role in the microstructure evolution during spinodal decomposition [14,15]. Indeed, the seminal work of Larche-Cahn has laid the foundation for describing the thermodynamics of stressed solids [16]. While CRs can suppress or shift the temperature range for phase transformation [12], mechanical fields can alter the equilibrium composition and equilibrium shape of coherent particles, change the coarsening process, and preferentially align composition in a direction parallel or perpendicular to an applied stress [17].

While experiments for the Mo-V binary system [11] have indicated a temperature range for spinodal decomposition, the impact of CRs, elastic inhomogeneity in terms of lattice parameter mismatch and inhomogeneous material properties, and externally applied stresses on the phase decomposition mechanisms has remained unrevealed. The natural next step is the use of computational modeling to go beyond the experimental considerations to understand the role of these effects on the kinetics of spinodal decomposition in the binary Mo-V alloy system. To the best of our knowledge, a detailed parametric study quantifying the effects of CRs, elastic inhomogeneity, and externally applied stresses on the spinodal decomposition of the Mo-V binary system has not been reported.

The phase-field method has been widely used for quantitative modeling of microstructure evolution and spinodal decomposition [18]. Arbitrary thermodynamic properties and kinetic parameters are frequently employed in phase-field formulations. To overcome this, the phase-field model has been either combined with the first-principles calculations to exclude arbitrariness in the material properties [19,20] or the CALPHAD (CALculation of PHAse Diagram [21]) approach to assess the thermodynamic properties of the system [22]. In this work, we formulate a multiscale framework by combining both the first-principles calculations and the CALPHAD approach with the phase-field method to simulate spinodal decomposition in the Mo-V binary system. The CALPHAD approach is used to obtain the Gibbs free energy density of the system as a function of composition and temperature. The interfacial energy, an important ingredient for microstructure evolution [23], and the elastic properties of the α and β phases are determined using the first-principles calculations. Special quasi-random structures (SQSs) are employed in the first-principles calculation to represent a random Mo-V alloy. This data is then fed into the phase-field model to simulate the microstructure evolution of the system within the miscibility gap region [11]. In addition to the two temperatures used in the experiment (873.15 K and 1023.15 K), a lower temperature of 700 K is also considered in this work. In addition to determining hitherto unavailable thermodynamic and material properties of the alloy, we study the role of temperature, cooling rates, and mechanical fields in microstructure evolution and morphology in elastically periodic arrays of the Mo-V binary system.

2. The phase-field model

The free energy functional F for a heterogeneous system occupying the domain V, with contributions from the chemical free energy density G^{loc}, interfacial free energy density Γ between the Mo-rich and V-rich phases, and elastic strain energy density $\in$ can be represented as

$$F = \int_V \left[G^{loc}(c_V, T) + \Gamma(\nabla c_V) + \in (\nabla u, c_V) \right] dV \tag{1}$$

where c_V is the vanadium composition (mole fraction) scalar field, T is the absolute temperature, and $\boldsymbol{u}$ is the displacement vector field.

2.1. Chemical free energy density

The chemical free energy density of the system $G^{loc}(c_V, T)$ is determined as a function of vanadium composition and temperature using the CALPHAD approach [21]. To address the deviation from ideal mixing and the dependence of excess free energy on temperature, we use the sub-regular solution model of the CALPHAD methodology to simulate the BCC solid solution phase of the Mo-V binary alloy system. The local Gibbs free energy density of the Mo-V system can be expressed as

$$G^{loc}(c_V, T) = \frac{1}{v_m}\left(G^{MM} + G^{ID} + G^{EX}\right) \tag{2}$$

where G^{MM}, G^{ID}, and G^{EX} are the Gibbs free energies in J/mol due to mechanical mixing, ideal term, and excess free energy, and v_m and is the molar volume. Each term is further decomposed as

$$G^{MM} = (1 - c_V)G^0_{Mo} + c_V G^0_V \tag{3}$$

$$G^{ID} = RT[(1 - c_V)\ln(1 - c_V) + c_V \ln c_V] \tag{4}$$

$$G^{EX} = (1 - c_V)c_V \sum_{n=0}^{n=i} L^n_{Mo,V}(1 - 2c_V)^n \tag{5}$$

where R is the universal gas constant and $L^n_{Mo,V}$ is the n^{th} interaction term between Mo and V in J/mol. In Eq. (3), G^0_{Mo} and G^0_V are the Gibbs free energies for pure Mo and pure V in the BCC phase obtained using experimental data in the Scientific Group Thermodata Europe (SGTE) database [24] (Supplementary Section 1).

The excess Gibbs free energy G^{EX} is modeled by a Redlich-Kister polynomial [25] such that n takes values from 0 to 2. Each interaction term is expressed as a function of temperature

$$L^n_{Mo,V} = b_0 + b_1 T \tag{6}$$

where b_0 and b_1 are the coefficients taken from recent experiments [11]

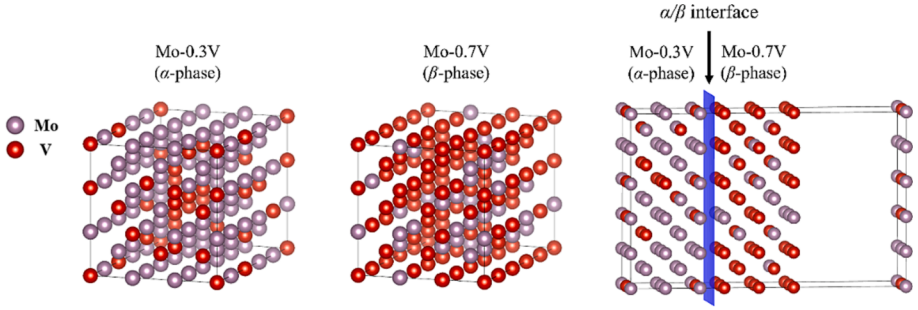

Fig. 1. An SQS supercell configuration of Mo-0.3V (α-phase), Mo-0.7V (β-phase) alloy, and a supercell configuration of the α/β interface.

as they have recently established the low-temperature miscibility gap boundary for the Mo-V binary alloy system. Expressions for G^0_{Mo} and G^0_V in Eq. (3) and each $L^n_{Mo,V}$ interaction term in Eq. (6) are given in Supplementary Section 1.

Combining Eqs. (2–6) renders the final expression for the chemical free energy of the system $G^{loc}(c_V, T)$ as a function of composition and temperature (Supplementary Section 1). A graphical representation of the chemical free energy with respect to the vanadium composition is given in Fig. 2(a) for the three temperatures considered (700 K, 873.15 K, and 1023.15 K). As these temperatures are within the miscibility gap range, as shown experimentally in Ref. [11], each plot in Fig. 2(a) exhibits a double-well potential curve. The equilibrium compositions of each phase are determined by constructing a common tangent to the Gibbs free energy curves. Fig. 2(b) show a magnified view of the Gibbs free energy at 700 K temperature and the corresponding common tangent. The common tangents to the Gibbs free energy at 873.15 K and 1023.15 K temperatures are presented in the Supplementary Fig. 1. The common tangent to the Gibbs free energy curves at 700 K and 873.15 K show the equilibrium compositions of the two stable phases are close to $c_V = 0.30$ and $c_V = 0.70$. Thus, the equilibrium alloys can empirically be written as $Mo_{1-x}V_x$ $(0.0 \le x \le 0.30)$ and Mo_yV_{1-y} $(0.0 \le y \le 0.30)$ for the Mo-rich and V-rich phases, respectively. The equilibrium compositions of the two stable phases at 873.15 K and 1023.15 K are in agreement with the experimentally reported equilibrium compositions [11].

2.2. Interfacial energy density

The first-principles calculations are conducted to obtain the interfacial energy between the two phases $\Gamma_{\alpha/\beta}$ and correlate it to the phase-field parameters. In that regard, we establish correlation functions, generate random SQSs, perform the first-principles calculations, and compute the interfacial energy. Once it is determined, the interfacial energy and the interface thickness are connected to the phase-field parameters [26].

2.2.1. Correlation functions and SQS

An interface is assumed between the α and β phases formed due to spinodal decomposition in the Mo-V alloy, as shown in Fig. 1. We use an SQS approach to generate Mo-V alloys with different vanadium compositions to mimic randomness in the system.

Considering a binary A-B system, the occupation of lattice sites can be expressed by the site occupation operator defined by p^j_i as

$$p^j_i = f(x) = \begin{cases} 1, & \text{if site } i \text{ is occupied by } A \\ 0, & \text{if site } i \text{ is occupied by } B \end{cases} \tag{7}$$

Similarly, we assign a spin, i.e., -1 or $+1$, to each lattice site using a site operator σ_i as

$$\sigma_i = p^B_i - p^A_i \tag{8}$$

Correlation functions of any cluster can be expressed as the average product of site operators of different sites in the cluster. Mathematically, it can be written as

$$\overline{\sigma}_k = \langle \sigma_1 \sigma_2 \sigma_3 \ldots \rangle \tag{9}$$

where $k = 1, 2, \ldots$ are different clusters, i.e., first-neighbor pair, second-neighbor pair, triangle, etc., which are expressed as a function of neighboring distances between clusters (d). $\overline{\sigma}_k$ provides an elegant way to characterize a structure based on its atomic configurations on different lattice sites. For an infinite random system, we expect complete randomness, i.e., there is no preference for the atomic occupation of any type of atom on any lattice site in the system. The correlation functions of an infinitely random system (R) can be expressed as

$$\langle \overline{\sigma}_{k,d} \rangle_R = (2x - 1)^k \tag{10}$$

It should be noted that the above correlation function becomes 0 when $x = 0.5$ (for a binary alloy system) except for $k = 0$, which indicates an empty cluster.

The generation of random configurations of a system for electronic structure calculations is important as the physical properties of the structure closely depend on its atomic arrangements [27]. Earlier theories based on random alloy configurations, such as virtual crystal approximation and site-coherent potential approximation, consider either the average occupation of different atoms on lattice sites or each atom is embedded equivalently in a uniform space [28]. SQSs are an attempt to create structures that best approximate the infinite version of its random alloy. Since SQSs are periodic structures, they cannot reproduce the correlation functions of their corresponding random system. Thus, the extent of randomness of SQSs is expressed as the departure of the correlation functions $\langle \overline{\sigma}_{k,d} \rangle_{SQS}$ to that from the corresponding infinitely random structure as

$$\varepsilon_{k,d} = \langle \overline{\sigma}_{k,d} \rangle_R - \langle \overline{\sigma}_{k,d} \rangle_{SQS} \tag{11}$$

We should expect that departure ($\varepsilon_{k,d}$) or error should be as low as possible. An improved methodology for SQS generation by minimizing error has been proposed in Ref. [29]. The method is based on a Monte Carlo simulated annealing loop in which an objective function (Q), primarily based on Eq. (11), is minimized iteratively

$$Q = -\omega L + \sum_{k \in C} |\varepsilon_{k,d}| \tag{12}$$

where C is a user-specified set of clusters, L is the largest length in cluster C such that $\varepsilon_{k,d}$ is 0, and ω is a user-specified weight (generally taken as

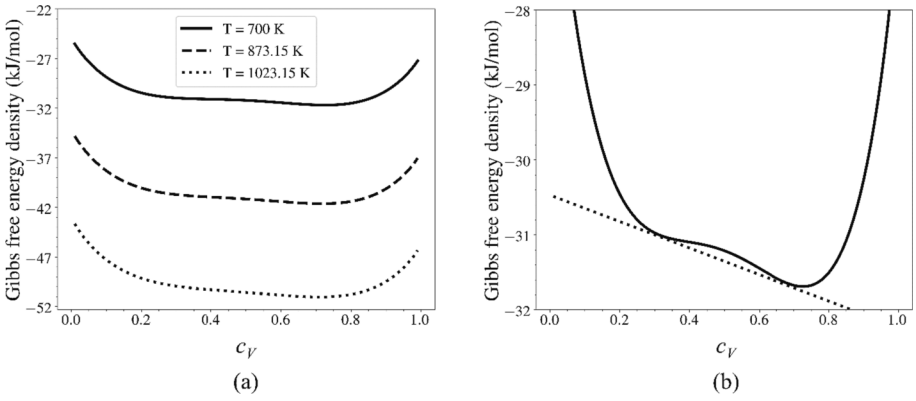

Fig. 2. (a) Gibbs free energy as a function of vanadium composition (c_V) at three different temperatures for the Mo-V binary alloy system [11] and (b) the common tangent at 700 K.

1). This methodology has been implemented in the Alloy Theoretic Automated Toolkit (ATAT) package [30] using the *mcsqs* module, which is used in the present paper to generate SQSs. During an SQS search, the cell dimensions are also allowed to change to mimic the random system. However, under certain conditions, one needs the cell dimensions not to change. The crystal structure of the generated SQS is restricted to the BCC system. This algorithm can also handle this constraint, and SQS can be generated iteratively without altering any cell dimension.

SQSs consisting of 40 atoms are generated at different vanadium compositions using a $5 \times 2 \times 2$ Mo-V alloy supercell. Since the generated SQSs are finite, their correlation functions cannot match perfectly with that of their corresponding random structures. Thus, there is an inherent difference between the correlation functions of SQSs and its corresponding random structures. Values of the objective function for each alloy and their corresponding errors in the first and second nearest neighbor correlation functions are listed in Supplementary Table 1. They are generated using the Monte-Carlo iterative scheme for SQS search by minimizing the objective function given in Eq. (12). It should be noted that the errors in the correlation functions of SQSs for Mo-0.5V are close to 0, and thus they adequately mimic random structures.

2.2.2. First-principles calculations

The first-principles total energy calculations are carried out for pure Mo, pure V, and each of the $5 \times 2 \times 2$ SQS supercell structures generated using all electron projector augmented wave method [31] implemented in the Vienna Ab-initio Simulation Package (VASP) [32]. The generalized gradient approximation [33] is used to model the exchange correlation in the system. After establishing the energy convergence, a plane-wave cut-off energy of 300 eV is used and a $4 \times 6 \times 6$ k-point mesh for Brillouin zone integration is constructed using the Monkhorst-Pack scheme [34]. The structures are relaxed using the conjugate-gradient method until the magnitude of forces acting on each atom and the external pressure from the stress tensor becomes lower than 0.005 eV/Å and 2 kB, respectively.

Fig. 1 shows the α and β SQS alloys close to the equilibrium alloys represented by the spinodal decomposition. To obtain the interfacial energy $\Gamma_{\alpha/\beta}$, a (0 0 1) interface between the α and β phase is constructed (Fig. 1), using a SQS supercell with 40 atoms in each phase. The lattice parameter of each system is approximated to the average lattice parameter obtained for the α and β phases from the first-principles calculation. Refer to Supplementary Fig. 2 for the variation of the lattice parameter with vanadium composition. For the interfacial energy calculation, a plane-wave cut-off energy of 300 eV is used with $4 \times 6 \times 1$ k-point mesh for Brillouin zone sampling.

2.2.3. Interfacial energy

The interfacial energy between the α and β phases ($\Gamma_{\alpha/\beta}$) is calculated using the following equation

$$\Gamma_{\alpha/\beta} = E_{\alpha/\beta} - \left[E_\alpha + E_\beta\right] - \left[E_\alpha^S + E_\beta^S\right] \tag{13}$$

In the above equation, $E_{\alpha/\beta}$ is the ground state total energy of the combined α and β phase configuration with the interface (Fig. 1), E_α and E_β are the formation energies of the α and β bulk phases shown in Fig. 1, and E_α^S and E_β^S are the surface energies of the α and β phases (Supplementary Fig. 3). Using the above equations, we compute the interfacial energy $\Gamma_{\alpha/\beta}$ for (0 0 1) surface to be 0.104 Jm^{-2}. The details regarding the first-principles calculations for determining the surface energies of the α and β phases are given in Supplementary Section 2. More accurate calculations of the planar fault energies employing different supercell sizes especially a larger supercell with clearly isolated images of the interface and free surfaces can yield more precise chemical and strain associated energies [35]. Further, the finite temperature contributions to the interfacial energy that arises due to possible atomic disorder (i.e., diffuse boundaries) and excess entropy (i.e., vibrational, thermo-electronic, etc.) also need to be considered. However, the present emphasis is on the microstructural evolution pertaining to spinodal decomposition and a comprehensive investigation of the interfacial energy is not within the scope of the study.

2.2.4. Phase-field parameters

The interfacial free energy density Γ in the total free energy functional (Eq. (1)) is expressed by the gradient of vanadium composition as

$$\Gamma(\nabla c_V) = \frac{1}{2}\kappa|\nabla c_V|^2 \tag{14}$$

where κ is the isotropic gradient energy coefficient expressed as [26]

$$\kappa = \frac{3}{4}\frac{\delta\Gamma_{\alpha/\beta}}{(\Delta c_V)^2} \tag{15}$$

where $\Gamma_{\alpha/\beta}$ is the interfacial energy calculated using Eq. (13), δ is the selected nominal interface thickness, and Δc_V is the difference in the equilibrium compositions in the Gibbs free energy density.

2.3. Elastic strain energy density

The elastic strain energy density is a quadratic form of the elastic strain ε^{el}, which is obtained by subtracting the stress-free strain (eigenstrain) ε_{eg} from the total strain ε. The eigenstrain tensor ε_{eg} includes compositional strains resulting from the difference in composition. Using c_{V0} as a reference composition for the stress-free state at equally mixed phases ($c_{V0} = 0.5$), the eigenstrain tensor reads [36]

$$\varepsilon_{eg}(c_V) = \eta(c_V - c_{V0})\mathbf{I}; \eta = \frac{a(c_V) - a_0(c_{V0})}{a_0(c_{V0})} \tag{16}$$

where η is the composition expansion/subtraction coefficient of the lattice parameter and $\mathbf{I}$ is the identity tensor. The η coefficient is expressed as the difference in stress-free (relaxed) lattice parameter $a(c_V)$ for a specific composition relative to the stress-free (relaxed) lattice parameter of the initial composition $a_0(c_{V0})$. The relaxed lattice parameter is obtained using the first principles calculations and given below in the text. We report that for the system considered and using the first principles results for the lattice parameter a, the coefficient η in Eq. (16) is $\eta = -1.12$ %. It is assumed that eigenstrain varies linearly with vanadium composition (Vegard's law), which is confirmed by employing the first principles calculations, and that compositional variations induce a pure dilation of the crystal lattice. The total strain tensor ε is the symmetric part of the displacement gradient

$$\varepsilon = \frac{1}{2}\left(\nabla\mathbf{u} + (\nabla\mathbf{u})^T\right). \tag{17}$$

Using Eqs. (16) and (17), the strain energy density is given as

$$\epsilon(\nabla\boldsymbol{u}, c_V) = \frac{1}{2}\varepsilon^{el} : \mathbf{C}(c_V) : \varepsilon^{el};\ \varepsilon^{el} = \varepsilon - \varepsilon_{eg}(c_V) \tag{18}$$

where $\mathbf{C}$ is the rank-four elastic stiffness tensor assumed to depend on the vanadium composition and vary between the Mo-rich and V-rich phases. For simplicity, we assume cubic symmetry and define the elastic stiffness tensor as

$$C_{ijkl} = C_{12}(c_V)\delta_{ij}\delta_{kl} + C_{44}(c_V)\left(\delta_{ik}\delta_{jl} + \delta_{il}\delta_{jk}\right) + \left(C_{11}(c_V) - C_{12}(c_V) - 2C_{44}(c_V)\right)\delta_{ijkl} \tag{19}$$

To complete the mathematical formulation, the lattice parameter $a(c_V)$ and the elastic constants C_{11}, C_{12}, and C_{44} as a function of vanadium composition are computed employing the first-principles calculations as described above. The lattice parameter variation, calculated from the relaxed structures as a function of c_V, as shown in Supplementary Fig. 2, varies closely with c_V according to Vegard's law. The obtained lattice

parameter dependence on composition is used to introduce the coefficient η and eigenstrains in Eq. (16). We emphasize that the results obtained for the lattice parameter are in agreement with Refs. [37,38].

The first-principles calculations are further utilized to determine hitherto unavailable elastic constants C_{11}, C_{12}, and C_{44} for the Mo-rich and V-rich phases. It is assumed in Eq. (19) that the elastic constants vary linearly with vanadium composition between the Mo-rich and V-rich phases. In addition to these elastic constants, material properties such as bulk modulus B, Young's modulus E, and shear modulus G that are not readily available in the literature for pure Mo, pure V, Mo-rich, and V-rich phases are computed. The determined material properties for the pure Mo and V phases agree well with the documented data in Refs. [39–42]. The obtained material properties are summarized in Table 1, while the details regarding the first-principles calculations for determining the material properties are given in Supplementary Section 3 and Supplementary Figs. 4–9.

2.4. Governing equations

Using the balance of power and the principle of virtual power [43] render the following time-dependent governing equations for the independent fields $c_V(\mathbf{x},t)$ and $\mathbf{u}(\mathbf{x},t)$

$$\left\{\begin{array}{c}\dfrac{\partial c_V}{\partial t}=\nabla\bullet M\nabla\left(\dfrac{\delta F}{\delta c_V}\right)=\nabla\bullet M\nabla\left(\dfrac{\partial G^{loc}}{\partial c_V}-\kappa\nabla^2 c_V+\dfrac{\partial\in(\nabla\boldsymbol{u},c_V)}{\partial c_V}\right)\\ \nabla\bullet\sigma=0\end{array}\right\} \tag{20}$$

where, σ is the Cauchy stress tensor defined as

$$\sigma_{ij}=\partial\in(\nabla\mathbf{u},c_V)/\partial\varepsilon_{ij}^{el} \tag{21}$$

while F is the total free energy functional of the system given in Eq. (1) and M is the kinetic coefficient that characterizes the vanadium composition mobility. The phase decomposition kinetics depend on the mobility parameter M which is given as

$$\begin{aligned}M&=\frac{\phi}{RT}\left[(1-c_V)D_v+c_V D_{Mo}\right]\\ \phi&=\frac{(1-c_V)c_V}{RT}\frac{\partial^2 G^{loc}}{\partial c_V^2}\end{aligned} \tag{22}$$

where ϕ is the thermodynamic factor that depends on temperature and composition, D_v and D_{Mo} the temperature-dependent self-diffusion constants for V and Mo determined using experimental data in Refs. [44,45]. For simplicity, it is assumed in the present paper that the thermodynamic factor ϕ and the mobility M are a function of composition only by fixing the temperature at 873.15 K. The variation of ϕ and M with composition at 873.15 K is shown in Supplementary Fig. 10.

2.5. Numerical implementation

The resulting set of partial differential equations (Eq. (20)) is implemented in the multi-physics finite element software package MOOSE [46]. The computational domain is a periodic cell [0, 500] × [0, 500] nm. Periodic boundary conditions are enforced on all edges. In addition, rigid body motion is prevented for the mechanical equilibrium equation. A structured mesh is generated using quadratic quadrilateral finite elements with a characteristic element size of 5 nm. The material properties and parameters common to all phase-field simulations are listed in Table 2.

The Cahn Hilliard equation (Eq. (20)) in its split form is used to solve for the microstructural evolution. The discretized form of equations is numerically solved through the Preconditioned Jacobian-Free Newton Krylov (PJFNK) method. Adaptive time stepping is used to adjust the timestep depending on the rate of solver convergence.

3. Results and discussion

All simulations are conducted for seventy days and at three temperatures within the miscibility gap region: 700 K, 873.15 K, and 1023.15 K. The role of temperature, cooling rates, compositional strain, and externally applied loading on the decomposition kinetics and the microstructure morphology in the binary Mo-V system is examined.

3.1. Isothermal treatment

We start the simulations using a Mo-0.5V alloy with an initial compositional fluctuation of ± 2% to mimic randomly occurring compositional variations in real systems. Fig. 3 depicts the phase-field predictions of microstructure evolution at different time intervals for the three temperatures considered, without any elastic energy contribution. The coarsening effect can be noticed for the three temperatures as the microstructure evolves with time. We observe a coarser microstructure when the alloy is treated isothermally for a longer time compared to a microstructure formed at a comparatively shorter time. Fig. 3 also reveals that increased temperature leads to coarser

Table 2
Parameters common to all phase-field simulations.

Quantity	Value	Unit	Remarks
Self-diffusion coefficient of Mo D_{Mo}	8.837×10^{-32}	m^2/s	[45]
Self-diffusion coefficient of V D_V	5.781×10^{-22}	m^2/s	[44]
Interfacial energy $\Gamma_{\alpha/\beta}$ Eq. (13)	0.104	J/m^2	This work
Gradient energy coefficient κ Eq. (15)	9.75×10^{-10}	J/m	This work
Composition expansion coefficient η Eq. (16)	−1.12 %	–	–
Phase-field mobility parameter M	Eq. (22)	m^2/s	–
Absolute temperature T	[700, 873.15, 1023.15]	K	–
Domain size	500 × 500	nm^2	–
Number of finite elements	100 × 100	–	–
Composition fluctuation	± 2 %	–	–
Elastic constant C_{11}^{α} in Mo-rich phase	348.48	GPa	This work
Elastic constant C_{12}^{α} in Mo-rich phase	203.42	GPa	This work
Elastic constant C_{44}^{α} in Mo-rich phase	85.88	GPa	This work
Elastic constant C_{11}^{β} in V-rich phase	203.81	GPa	This work
Elastic constant C_{12}^{β} in V-rich phase	108.94	GPa	This work
Elastic constant C_{44}^{β} in V-rich phase	37.94	GPa	This work

Table 1
Material properties of pure Mo, pure V, Mo-0.3V, and Mo-0.7V phases determined using the first-principles calculations.

System	B(GPa)	C_{11}(GPa)	C_{12}(GPa)	C_{44}(GPa)	E(GPa)	G(GPa)
Pure Mo	276.7 (236[a], 275[b])	433.87 (407.8[a], 450[c])	198.11 (150[a], 176[d])	128.56 (135.5[a], 125[c])	324.29 (335.3[a])	124.29 (132.7[a])
Pure V	195.5 (159.7[a], 194[b])	276.42 (261[a], 232[c])	155.03 (130[c])	43.04 (45.5[a], 46[c])	138.48 (154[a], 127.6[d])	50.1 (57.6[a], 46.7[d])
Mo-0.3V	251.77	348.48	203.41	85.88	218.34	80.54
Mo-0.7V	210.85	203.81	108.94	37.94	117.46	41.74

[a] Reference [40]. [b] Reference [39]. [c] Reference [42]. [d] Reference [41].

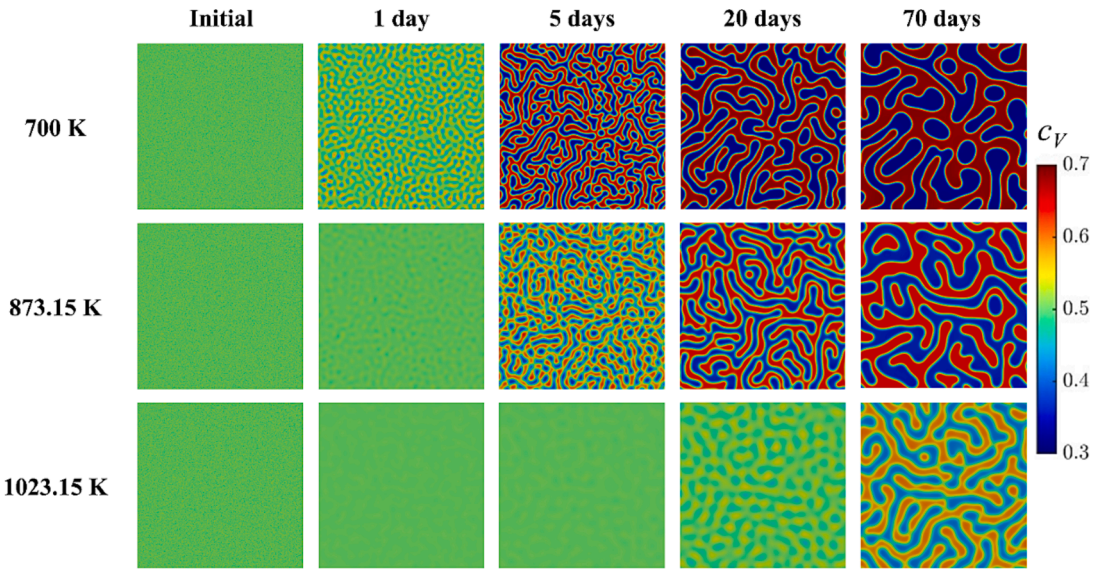

Fig. 3. Time evolution of phase-field generated microstructures of spinodal decomposition in the Mo-V binary alloy isothermally treated at different temperatures.

microstructures. For instance, at the end of the seventy-day simulation period, the microstructure at 1023.15 K is relatively coarser than the corresponding microstructures at 700 K or 873.15 K. SEM images of Mo-V alloy treated isothermally at 873.15 K and 1023.15 K from Ref. [11] are shown in Fig. 4 for the sake of comparison. Bcc(Mo, V)1 and Bcc(Mo, V)2 represent Mo-rich and V-rich phases formed after spinodal decomposition in the system.

In addition to the coarsening effect, the temperature alters the equilibrium composition of the α and β phases at the end of the simulation period. As illustrated in Fig. 3, the equilibrium compositions of the two phases at 700 K at the end of the seventy-day simulation period are $c_V = 0.30$ and $c_V = 0.70$. Spinodal decomposition starts after approximately one day at the same temperature. In the case of 873.15 K, the phase equilibrium compositions are slightly altered and closer to $c_V = 0.35$ and $c_V = 0.65$, and spinodal decomposition is suppressed for up to 2.4 days. In comparison, the equilibrium composition of the α and β phases at 873.15 K, as shown in Fig. 4, are $c_V = 0.38$ and $c_V = 0.62$, which is close to the simulation results. A similar trend is observed for the system at 1023.15 K, in which spinodal decomposition starts after 17.7 days with equilibrium compositions $c_V = 0.40$ and $c_V = 0.60$, as indicated in Fig. 3. Correspondingly, when compared with Fig. 4 for 1023.15 K, the equilibrium compositions are $c_V = 0.44$ and $c_V = 0.56$ for the α and β phases.

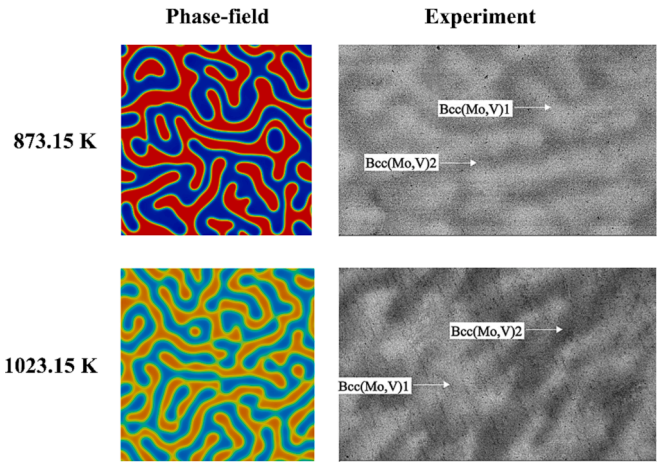

Fig. 4. Evolved microstructures of the Mo-V alloy isothermally treated for 70 days at 873.15 K and 1023.15 K. The SEM images are taken from Ref. [11]. Bcc (Mo,V)1 and Bcc(Mo,V)2 stand for Mo-rich and V-rich phases.

The free energy density of the system at the three temperatures considered rapidly decreases with time, indicating spinodal decomposition as a thermodynamically favorable mechanism for phase transformation. The Gibbs free energy density variation with time for seventy days at 700 K is given in Supplementary Fig. 11(a). A similar S-shaped curve can be obtained for the system at 873.15 K and 1023.15 K. Supplementary Fig. 11(b) shows the amount of the β phase formed at the three temperatures. In the case of 700 K and 873.15 K, the amount of the β phase formed initially increases rapidly, followed by a decline in phase formation, and finally, it reaches a plateau for longer simulation times. At the end of the seventy-day simulation period, the fraction of β phase is 0.45 and 0.42 at 700 K and 873.15 K. As could be observed in Supplementary Fig. 11, a negligible increase in the β phase and the chemical free energy density G^{loc} (Supplementary Table 2) is obtained after a thirty-day simulation period at 700 K and 873.15 K temperatures. Thus, the most significant amount of the β phase is formed within the first thirty-day simulation period. On the other hand, different spinodal decomposition kinetics is returned at 1023.15 K. As depicted in Fig. 3 and Supplementary Fig. 11(b), phase decomposition is entirely suppressed with no β phase present at this temperature for approximately twenty days. After that point, the formation of the β phase slowly increases to forty days and slows down afterward to reach a plateau at sixty days. Further increase in simulation time returns no significant increase in the β phase. At the end of the seventy-day simulation period, the fraction of β phase is 0.35 at 1023.15 K.

3.2. *Effect of cooling*

We study the effect of cooling on the microstructure evolution in the Mo-0.5V binary alloy cooled from a high initial temperature of 1500 K to 700 K using different cooling rates, i.e., 0.1 K/hr, 0.25 K/hr, 0.5 K/hr, and 1.0 K/hr. For each case, the microstructure is reported at 1023.15 K, 873.15 K, 750 K, and 700 K to show the effect of CRs on the spinodal decomposition kinetics. It is worth noting that the nucleation-and-growth mechanism can be triggered when the alloy composition falls outside the spinodal region but within the common tangent region. However, in this study, only spinodal decomposition is relevant to all the considered starting compositions. Therefore, the nucleation-and-growth mechanism is not the focus of this work.

The first case study includes cooling the alloy from the initial tem-

perature (1500 K) to the final temperature of 700 K at 0.1 K/hr CR. In this case, spinodal decomposition is observed after 231 days and at 945 K, Fig. 5. At the end of the cooling period at 700 K, the fraction of β phase formed in the system is 0.44. In the second case, a CR of 0.25 K/hr is used to cool the system from the same initial temperature to the final temperature. Starting from the single phase at 1500 K, the system is cooled linearly and it takes 133.3 days for the cooling to complete. During this cooling process, spinodal decomposition triggers after 102 days at 890 K and the system decomposes into two phases, Fig. 5. The fraction of β phase formed in the system at the end of the cooling period is 0.42. In the third case, CR is increased to 0.5 K/hr, which further suppresses the temperature range for spinodal decomposition. It takes approximately 67 days to cool the system while spinodal decomposition triggers after 55 days at 845 K, Fig. 5. After cooling at 0.5 K/hr, the fraction of β phase formed in the system is 0.41. Finally, in the fourth case, a further increase in the CR to 1 K/hr suppresses the spinodal decomposition temperature as well as time to 777 K and 30 days, in a cooling period of 33.3 days, respectively. In this case, the amount of β phase formed in the system at the end of the cooling period is 0.39.

Fig. 5 shows the microstructure evolution for the four cooling rates considered. It should be noted that the amount of β phase formed at the end of the cooling period decreases in the system with an increase in the CR. For any CR considered, microstructure coarsening is observed at lower temperatures as cooling progresses in the system. As shown in Fig. 5, spinodal decomposition can be entirely suppressed by cooling a Mo-0.5V alloy from 1500 K to 1023.15 K at all four cooling rates considered. However, spinodal decomposition can be induced by further cooling to the final temperature of 700 K.

The obtained results in Fig. 5 indicate that there is a critical cooling rate at which spinodal decomposition is fully suppressed in the temperature range considered. To achieve this, the CR is further increased in the simulations until the single-phase alloy is reached. Fig. 6 depicts different CRs and the onset of spinodal decomposition in the system for each case considered. In the case of slow cooling at 0.1 K/hr, a single-phase Mo-0.5V random alloy is exposed to longer cooling times and its decomposition into the two phases is more feasible. In this case, spinodal decomposition occurs when the temperature drops below the miscibility gap limit. Increasing the cooling rates shortens the exposure time within the miscibility gap. As a consequence, the temperature at which spinodal decomposition occurs is reduced. In the case of fast cooling, the single-phase alloy has insufficient time to decompose into two phases. At a CR of 2.2 K/hr, it is observed that the single phase misses the spinodal decomposition and retains a single phase at the end of the cooling period. This CR is the critical CR of the system above which spinodal decomposition does not take place, as shown in Fig. 6. The grey-shaded region in Fig. 6 stands for the area in which the spinodal decomposition of the system occurs, whereas the white region indicates the single-phase alloy. The single and two-phase regions are separated by a decomposition boundary.

3.3. Effect of elasticity

The effect of inhomogeneous elasticity due to the compositional inhomogeneity and the application of external stresses are analyzed by activating the coupling between the temporal evolution for c_V and mechanical stresses. It is emphasized that the previous simulations (Section 3.1 and Section 3.2) do not account for the mechanical contribution. Even though this is an idealized case, it serves to isolate the effect of elasticity on microstructure evolution. It is further assumed that the elastic effects do not affect the interfacial energy and thickness.

We assume cubic symmetry in the simulation and consider periodic structures as in the previous case studies. The material properties of pure Mo, pure V, α, and β phases are given in Table 1. Two case studies are considered. First, we examine the role of compositionally-generated elastic stresses on spinodal decomposition kinetics. The second case study extends the previous one by applying uniaxial tensile strains in the horizontal direction. In both case studies, the three representative temperatures, i.e., 700 K, 873.15 K, and 1023.15 K, are considered and the alloy is treated isothermally at these temperatures. We note that the effect of the CR is not considered while examining the elastic effects.

3.3.1. Effect of compositional strain

Compositionally-generated elastic stresses directly affect the development of spinodal decomposition and microstructure morphology in

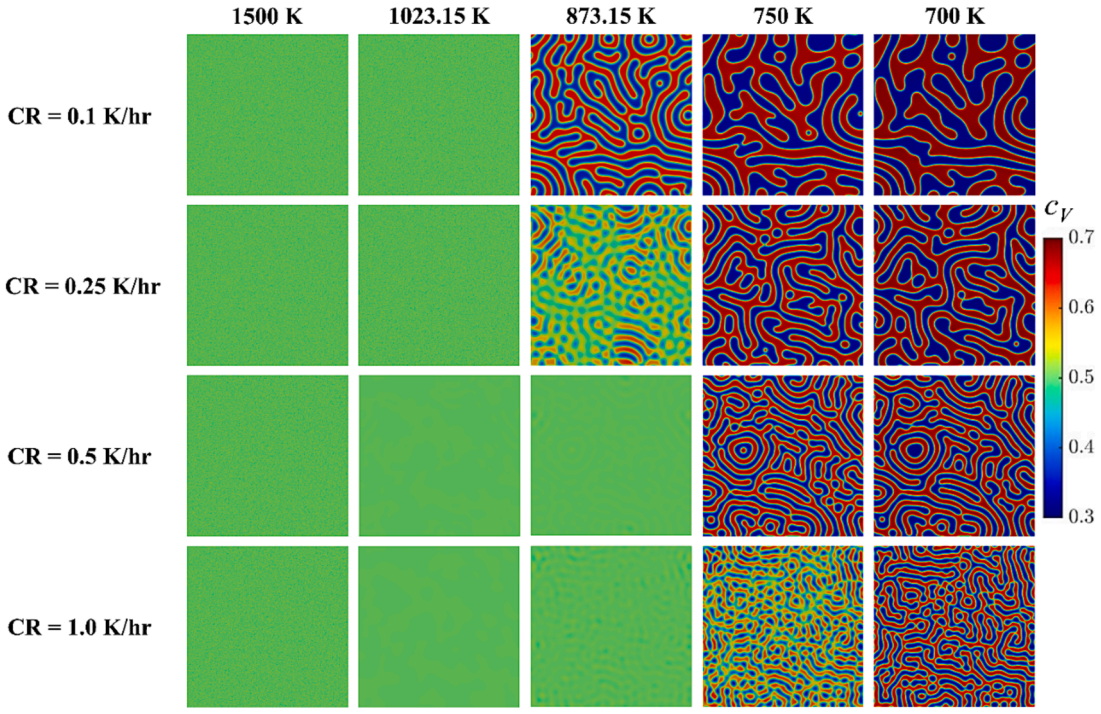

Fig. 5. Phase-field simulated microstructures on cooling a Mo-0.5V alloy from 1500 K at different cooling rates (CRs).

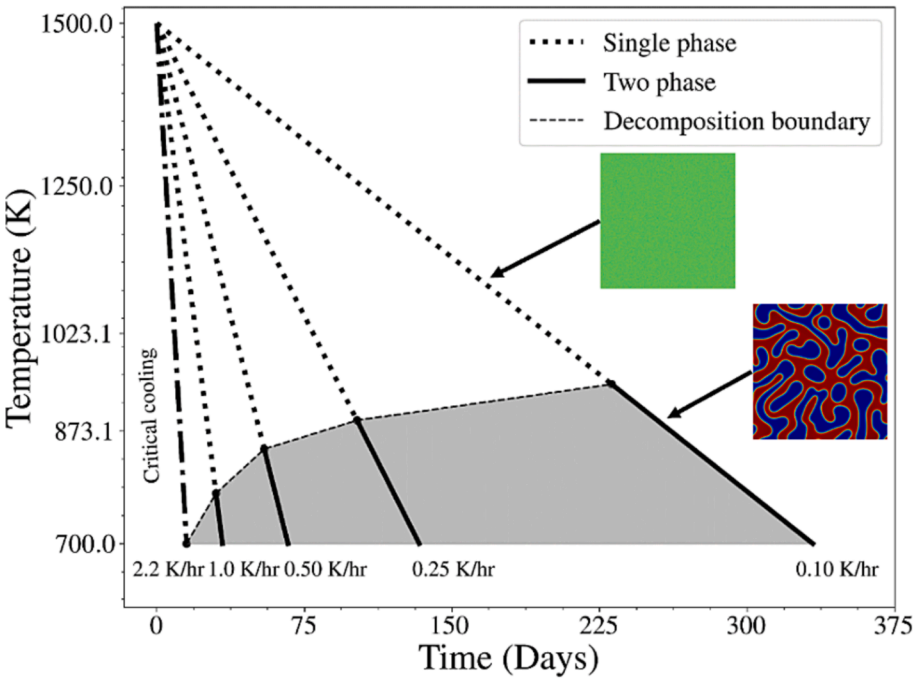

Fig. 6. Continuous cooling transformation diagram for the Mo-V binary alloy system.

the Mo-V binary system, Fig. 7. In the case of low temperature (700 K), the system is decomposed into the α and β phases. Yet, the decomposition kinetics and amount of the β phase formed are altered compared to the case without compositional strains (Fig. 3). Moreover, the elastic effects change the minimum composition of c_V for the spinodal decomposition. The equilibrium compositions of the α and β phases are slightly changed and shifted to $0.32c_V$ and $0.68c_V$; without the compositional effect, the equilibrium compositions are at $0.3c_V$ and $0.7c_V$.

For the moderate and high temperatures (873.15 and 1023.15 K), the effect of compositional elastic stresses on the decomposition kinetics and the microstructure morphology is even more pronounced, Fig. 7. In the case of 873.15 K, the system decomposes into the α and β phases with the equilibrium composition of $0.35c_V$ and $0.64c_V$. However, in the case of high temperature (1023.15 K), the elastic compositional effects further suppress the decomposition kinetics and no spinodal decomposition occurs for the simulation period considered.

The behavior of the phase-field model in the presence of compositional stress can be understood in the context of the work of Cahn and Larché on coherent equilibrium of two-phase solid solutions [47]. That work predicts a reduction in the two-phase compositional field as elastic energy resulting from composition-dependent interfacial coherence increases. This behavior is consistent with our observations of a change in equilibrium compositions of the α and β phases, for instance, to $0.32c_V$ and $0.68c_V$ at 700 K; compared to the equilibrium composition of $0.3c_V$ and $0.7c_V$ without the compositional effect. Cahn and Larché's model also predicts the possibility of elastic energy eliminating the two-phase equilibrium by favoring single-phase equilibrium. This later behavior is also consistent with our observations in Fig. 7.

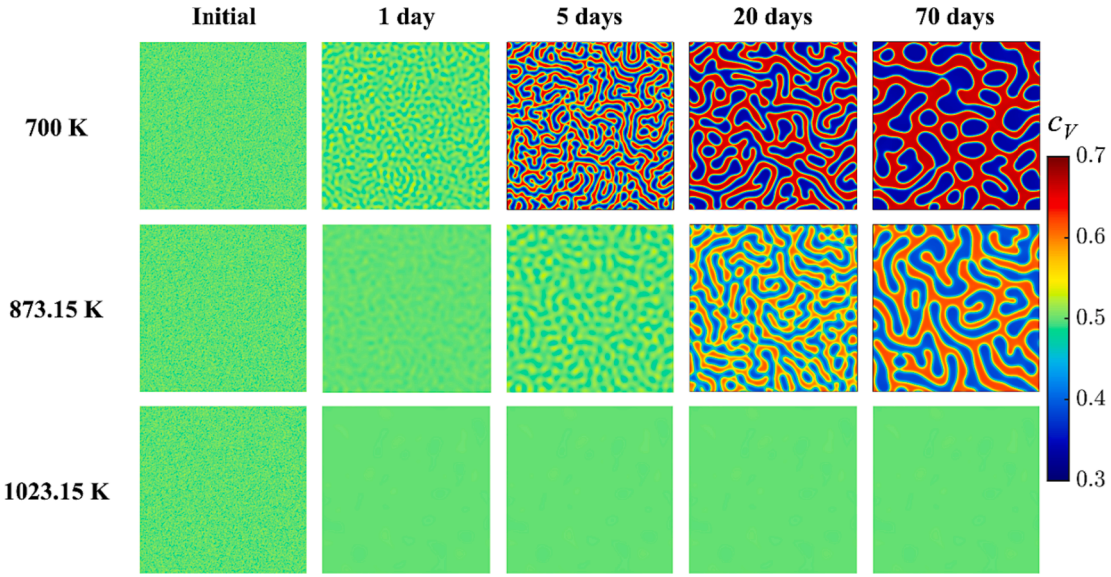

Fig. 7. Time evolution of phase-field generated microstructures of spinodal decomposition in the Mo-V binary alloy isothermally treated considering compositional elastic effects at different temperatures.

To shed light on the latter behavior, let us consider a simple model of two solid binary solid solutions, α and β in equilibrium with each other (same chemical constituents, chemical species 1 and 2)) at constant hydrostatic pressure. The Gibbs free energy of the composite system is given in its molar form by

$$G\left(Z, x_1^{\alpha}, x_1^{\beta}\right) = ZG^{\alpha}\left(x_1^{\alpha}\right) + (1-Z)G^{\beta}\left(x_1^{\beta}\right) \tag{23}$$

where Z is the mole fraction of α phase, and $(1-Z)$ the mole fraction of β phase. x_1^{α} and x_1^{β} are the mole fractions of chemical component 1 in the two phases. We simplify the model further by considering the Gibbs free energies of two stable phases α and β are symmetrical about the composition $x = 0.5$ and that $G^{\alpha}\left(x_1^{\alpha,e}\right) = G^{\beta}\left(x_1^{\beta,e}\right) = G_0$, where $x_1^{\alpha,e}$ and $x_1^{\beta,e}$ are the equilibrium compositions for the two phases. This is not the case for the Mo-V system but this does not impact the conclusion of this argument. We also limit this problem to mixtures with overall composition $x = 0.5$. We now assume that the compositional elastic energy adds an energy term to Eq. (23) of the form

$$E = AZ(1-Z) \tag{24}$$

where A is a positive constant. Assuming that $x_1^{\alpha,e}$ and $x_1^{\beta,e}$ do not depend on A. At $x = 0.5$, because of the symmetry of the molar free energies, at equilibrium $Z = 0.5$ and the elastic energy becomes $E(x = 0.5) = \frac{A}{4}$. At $x = 0.5$, $G = \frac{1}{2}G^{\alpha} + \frac{1}{2}G^{\beta} = G_0$. A two-phase system with compositional stress will therefore have free energy given by $G + E = G_0 + \frac{A}{4}$. The free energy of pure phases at $x = 0.5$ are $G^{\alpha}(x = 0.5) = G^{\beta}(x = 0.5) = G_p$ with $G_p > G_0$. Since G_p does not depend on A, there is a threshold, $A_T = 4\left(G_p - G_0\right)$ below which the two-phase system is more stable than the individual single phases but above which the single phases are more stable than the phase-separated system. This behavior may therefore explain the observation of the absence of separation (i.e., retaining a single phase) in the phase-field model simulations in the presence of compositional stress.

3.3.2. Effect of applied strain

Since the elastic compositional stresses entirely suppress phase decomposition at 1023.15 K, we examine the role of applied loading at 700 K and 873.15 K. Fig. 8 depicts the phase-field predictions in terms of microstructure evolution for three different applied tensile uniaxial strains. Small external strains (0.1%) do not significantly affect spinodal decomposition kinetics and microstructure morphology, and similar results are returned as in the previous case with compositionally-generated elastic stresses. The system returns the same equilibrium compositions and the amount of the β phase as in the compositional strain case at 700 K (Fig. 7). Both phases are continuous with no directional alignment.

Imposing higher strains (e.g., 0.5% and 1%) affects the microstructure morphology, Fig. 8. Yet, similar equilibrium compositions are returned as for the 0.1% external strain case or the system with only compositional strains. The formed phases are elongated and aligned parallel to the direction of the applied uniaxial strains, leading to directional phase separation. This effect is particularly noticeable for high external loads and can be observed by comparing the 0.1% and 1% strain cases. The magnitude of the applied strains determines the degree of alignment, Fig. 8. As the applied strain increases, the alignment shifts toward the horizontal direction and returns even more parallel domains. Similar observations for directional phase separation have been reported elsewhere for similar systems [15,48].

In the case of higher temperatures (873.15 K), the spinodal decomposition is delayed up to 20 days for all three external strains considered, Fig. 9. Once the phases are formed, they follow the same behavior and directional precipitation alignment with an increase in the applied strain as in the previous case at 700 K. Comparing Figs. 7, 8, and 9 one can observe that compositional stresses determine the time required for the spinodal decomposition formation while externally applied strains alter microstructure morphologies and produce directional precipitation alignment. Moreover, externally applied strains do not affect the equilibrium compositions of the α and β phases.

The following condition can be used to determine the direction of precipitation alignment [49]

$$\begin{aligned} &\sigma\varepsilon_{eg}(1-\xi) < 0, \text{ alignment parallel to the load direction} \\ &\sigma\varepsilon_{eg}(1-\xi) > 0, \text{ alignment perpendicular to the load direction} \end{aligned} \tag{25}$$

As seen in Eq. (25), the elastic inhomogeneity $\xi = \frac{C_{44}^{\beta}}{C_{44}^{\alpha}}$ is the necessary condition to initiate the directional alignment in a microstructure. If both phases have the same elastic constants, the directional phase separation does not occur, regardless of the magnitude of the applied stress or eigenstrain (ε_{eg}). Using the values in Table 1 for C_{44}^{β} and C_{44}^{α} one can obtain that in the present case $\xi < 1$. As the eigenstrain value $\varepsilon_{eg} < 0$, Eq. (16), the alignment parallel to the load direction is restored for the case study considered. The applied stress (σ) also controls the microstructure morphology and determines the degree of alignment. The greater the difference in the elastic properties and applied stress, the higher the degree of alignment. It is emphasized that the material properties of V-rich C_{44}^{β} and Mo-rich phases C_{44}^{α}, which are essential for determining directional phase separation in the Mo-V binary system, have not been

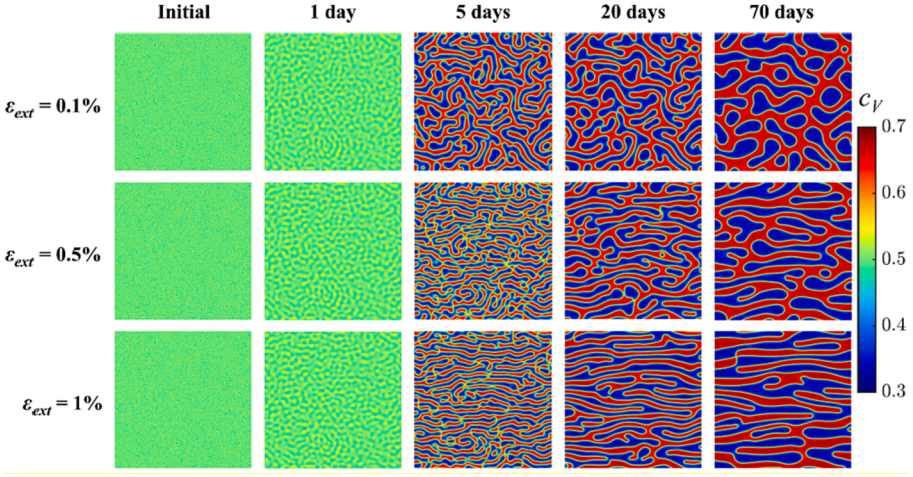

Fig. 8. Time evolution of phase-field generated microstructures of spinodal decomposition in the Mo-V binary alloy isothermally treated for various external strains at 700 K.

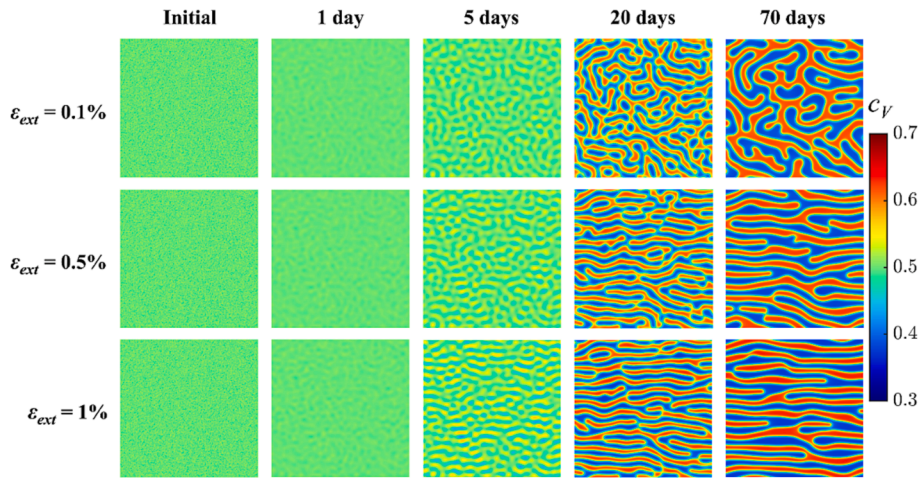

Fig. 9. Time evolution of phase-field generated microstructures of spinodal decomposition in the Mo-V binary alloy isothermally treated for various external strains at 873.15 K.

reported in the literature. These properties are computed in the present work using the first principles calculations.

3.4. Summary and future work

A first-principles and CALPHAD informed phase-field model to simulate the effect of temperature, cooling rates, and mechanical fields on spinodal decomposition in elastically periodic arrays of the Mo-V binary system is developed in this work. Phase-field simulations regarding isothermal treatment predict coarse microstructures as time progresses at each temperature considered. Higher temperatures delay the spinodal decomposition in the system and affect the equilibrium composition of the pure phases. The obtained results reveal that a critical cooling rate of 2.2 K/hr fully suppresses spinodal decomposition in the system. A cooling rate smaller than the critical cooling rate triggers spinodal decomposition. In addition, compositionally-generated elastic stresses affect the development of spinodal decomposition and microstructure morphology. High temperatures, in combination with compositional stresses, suppress the decomposition kinetics and no spinodal decomposition occurs. Applying external loading in the Mo-V binary system leads to directional precipitation alignment parallel to the load direction. The elastic inhomogeneity in terms of material properties between the two phases initiates the directional alignment, while eigenstrains and applied external loading control the degree of alignment.

The present model is based on a thermodynamic free energy functional that incorporates chemical, gradient, and mechanical contributions, as given in Eq. (1). Phase-field models typically contain some arbitrariness in terms of thermodynamic data, material properties, and model parameters, which can affect microstructure evolution. In the current phase-field model, the chemical contribution is built upon experimental thermodynamic data of the pure phases [24] and an optimized phase diagram of the system using experiments in Ref. [11]. This enables us to define the spinodal boundary for a given temperature and composition range based on experimental data. An arbitrary chemical energy definition may exclude the presence of a miscibility gap boundary in the Mo-V phase diagram and even lead to no phase separation. The gradient energy, an energy penalty associated with gradients in vanadium composition, is expressed as a function of phase-field parameter κ, Eq. (14). This model parameter is dependent on the interfacial energy between the α and β phases (Eq. (15)), which to the best of our knowledge, has not been reported in the literature. In this investigation, the interfacial energy is determined using the first-principles calculations. The elastic constants of the α and β phases and the eigenstrain coefficient constitute the mechanical contribution in the free energy functional, Eq. (18). Although the eigenstrain coefficient has been reported in the literature [37,38], the present paper determines for the first time the elastic constants of the two phases using the first-principles calculations. As given in Eq. (25), the elastic inhomogeneity, the ratio between the elastic properties of the two phases, is the essential condition for directional phase separation. The results in Fig. 8 and Fig. 9 demonstrate that the system considered exhibits directional alignment parallel to the applied loading. Inaccurate estimation or assuming the same elastic constant of the two phases would result in opposite behavior or microstructures with no directional alignment. In addition, the phase-field mobility parameter, which governs the kinetics of the interface, is associated with the self-diffusion coefficients of Mo and V and the thermodynamic factor, which is dependent on the chemical contribution, Eq. (22). Thus, these three energy ingredients in Eq. (1) play a significant role in governing the kinetics of microstructure evolution and determining microstructure morphology. In the present model, they are formulated using experimental thermodynamic data or the first-principles calculations to accurately capture the behavior of the Mo-V system.

The multiscale computational framework developed can assist in predicting the microstructure evolution of steel alloys subjected to various manufacturing and service conditions. The model may serve as a complementary tool for designing enhanced steel alloys with desired material properties. Although the current work focuses on the Mo-V subsystem, the framework developed is general and extendable to ternary sub-systems in steel alloys.

The availability to foresee the microstructure morphology in alloys under various cooling rates and external stresses is appealing for practical applications in the design of steel alloys. The present work can be utilized in design principles of high entropy alloys containing Mo and V and extended to model the microstructure evolution in multicomponent systems by including the Gibbs energy description of higher-order systems frequently employed in industrial applications. The framework developed can also assist in creating databases for surrogate neural network [50], time series Long Short-Term Memory (LSTM) models [51], and phase diagrams [52] that can aid in predicting microstructure evolution utilizing lower computational cost and laying out the microstructure spectra at different processing and service conditions, which is ultimately beneficial in the alloy design.

Future work should include non-periodic multigrain assemblies, incorporating the role of grain boundary, dislocations, and plasticity on phase separation in the Mo-V binary system. The incorporation of ternary, quaternary, and other higher multicomponent sub-systems in steel alloys should also be considered in future work.

4. Conclusions

A multiscale computational framework based on the CALPHAD, the first-principles calculations, and the phase-field method is presented for assessing the microstructure evolution in the Mo-V binary alloy. Built upon recent experiments, three different temperatures within the miscibility gap region (700 K, 873.15 K, and 1023.15 K) are selected to determine the thermodynamic properties of the alloy. The first-principles calculations and the CALPHAD approach are used to obtain the material properties and free energies of the system that are fed into the phase-field model to track microstructure evolution. The main findings can be summarized as follows:

- Temperature affects the microstructure morphology and the equilibrium compositions. Increasing temperature leads to more coarse microstructures and a smaller difference between the equilibrium composition of the α and β phases formed.
- Temperature directly influences the amount of the V-rich phase formed. The lower the temperature, the more V-rich phase is formed. For isothermal treatment at 700 K and 873.15 K, the fraction of the β phase formed is 0.45 and 0.42 respectively, at the end of seventy days. In comparison, the fraction of the β phase is 0.35 at the end of seventy days for isothermal treatment at 1023.15 K.
- Temperature also influences the time for spinodal decomposition in the system. For isothermal treatment at 700 K, it takes one day for the system to start decomposing into α and β phases, while it takes 2.4 days for the same at 873.15 K. Further, it takes 17.7 days to observe the spinodal decomposition in the system when the alloy is isothermally treated at 1023.15 K.
- Cooling rates have a significant impact on spinodal decomposition. Rapid cooling rates can entirely suppress the spinodal process and alter the onset of phase separation. Slower cooling rates return more coarse microstructures and more pronounced formation of the V-rich phase.
- There is a critical cooling rate associated with spinodal decomposition in the system. A cooling rate higher than a critical cooling rate of 2.2 K/hr will suppress the phase separation in the system entirely. On the other hand, a cooling rate lower than the critical cooling rate will result in the phase separation into Mo-rich and V-rich phases.
- We found that inhomogeneous elasticity induced by compositional elastic stresses alters the decomposition kinetics and minimum composition for spinodal decomposition. The compositionally-generated elastic stresses at high temperatures fully suppress the decomposition process.
- Higher external uniaxial tensile strains (e.g., 0.5% and 1%) affect the microstructure morphology. However, they do not influence the equilibrium compositions and the amount of the β phase formed. High uniaxially applied strains (e.g., 1%) produce directional microstructures. The elastic inhomogeneity, a ratio between the material properties in the Mo-rich and V-rich phases, triggers the directional alignment. The system exhibits directional phase separation parallel to the direction of the applied uniaxial strain. The magnitude of applied stresses and eigenstrains determines the degree of alignment.

Author contributions

A.K.T. and S.K. conceptualized and directed this research, performed all the simulations, and wrote the initial manuscript draft. V.R.M., P.A. D., and K.M. supervised the study. All authors contributed to interpreting the data and preparing and editing the manuscript.

6. Code availability

Code available on request from the authors.

Declaration of Competing Interest

The authors declare that they have no known competing financial interests or personal relationships that could have appeared to influence the work reported in this paper.

Data availability

Data will be made available on request.

Acknowledgments

The authors sincerely thank Bradford Westrom, Chief Metallurgist, Freeport McMoRan, El Paso TX, USA, for many valuable discussions and insights. Calculations are performed utilizing High Performance Computing (HPC) resources supported by the University of Arizona TRIF, UITS, and Research, Innovation, and Impact (RII) and maintained by the UArizona Research Technologies department.

Appendix A. Supplementary data

Supplementary data to this article can be found online at https://doi.org/10.1016/j.matdes.2023.112443.

References

[1] C.C. Tasan, M. Diehl, D. Yan, M. Bechtold, F. Roters, L. Schemmann, C. Zheng, N. Peranio, D. Ponge, M. Koyama, K. Tsuzaki, D. Raabe, An Overview of Dual-Phase Steels: Advances in Microstructure-Oriented Processing and Micromechanically Guided Design, Annu. Rev. Mater. Res. 45 (2015) 391–431, https://doi.org/10.1146/annurev-matsci-070214-021103.
[2] D. Ikeuchi, D.J.M. King, K.J. Laws, A.J. Knowles, R.D. Aughterson, G.R. Lumpkin, E.G. Obbard, Cr-Mo-V-W: A new refractory and transition metal high-entropy alloy system, Scr. Mater. 158 (2019) 141–145, https://doi.org/10.1016/j.scriptamat.2018.08.045.
[3] M.R. Suresh, 0.3C–CrMoV(ESR) Steel: A New Ultrahigh Strength Steel, Trans. Indian Inst. Met. 64 (2011) 483–492, https://doi.org/10.1007/s12666-011-0074-9.
[4] Applications of vanadium in the steel industry, Vanadium (2021) 267–332, https://doi.org/10.1016/B978-0-12-818898-9.00011-5.
[5] M. Godec, S. Malej, D. Feizpour, M. Donik, D. Balažic, L. Klobčar, M. Pambaguian, A.K. Conradi, Hybrid additive manufacturing of Inconel 718 for future space applications, Mater. Charact. 172 (2021), 110842, https://doi.org/10.1016/J.MATCHAR.2020.110842.
[6] M. Hunkel, Segregations in Steels during Heat Treatment - A Consideration along the Process Chain, HTM J. Heat Treat. Mater. 76 (2021) 79–104. https://doi.org/doi:10.1515/htm-2020-0006.
[7] E. Rudy, Ternary phase equilibria in transition metal-boron-carbon-silicon systems. part 5. compendium of phase diagram data, 1969. https://www.osti.gov/biblio/4754828.
[8] J.F. Smith, The mo-v system (molybdenum-vanadium), J. Phase Equilibria 13 (1992) 50–53, https://doi.org/10.1007/BF02645376.
[9] F. Zheng, B.B. Argent, J.F. Smith, Thermodynamic computation of the Mo-V binary phase diagram, J. Phase Equilibria 20 (1999) 370, https://doi.org/10.1361/105497199770340897.
[10] J. Bratberg, K. Frisk, A thermodynamic analysis of the Mo-V and Mo-V-C system, Calphad. 26 (2002) 459–476, https://doi.org/10.1016/S0364-5916(02)00057-3.
[11] W. Yang, Z. Gao, C. Li, C. Guo, Z. Du, Experimental measurement and thermodynamic optimization on the solidus miscibility gap of the Mo-V binary and the Mo-Nb-V ternary systems, J. Alloys Compd. 857 (2021), 157509, https://doi.org/10.1016/J.JALLCOM.2020.157509.
[12] Z.Q. Bu, Y.G. Zhang, L. Yang, J.M. Kang, J.F. Li, Effect of cooling rate on phase transformation in Ti2AlNb alloy, J. Alloys Compd. 893 (2022), 162364, https://doi.org/10.1016/J.JALLCOM.2021.162364.
[13] F.P. Duda, G. Tomassetti, On the Effect of Elastic Distortions on the Kinetics of Diffusion-Induced Phase Transformations, J. Elast. 122 (2016) 179–195, https://doi.org/10.1007/s10659-015-9539-0.
[14] J.W. Cahn, On spinodal decomposition, Acta Metall. 9 (1961) 795–801, https://doi.org/10.1016/0001-6160(61)90182-1.
[15] D.J. Seol, S.Y. Hu, K.H. Oh, L.Q. Chen, Effect of substrate constraint on spinodal decomposition in an elastically inhomogeneous thin film, Met. Mater. Int. 10 (2004) 429–434, https://doi.org/10.1007/BF03027344.
[16] F. Larché, J.W. Cahn, A linear theory of thermochemical equilibrium of solids under stress, Acta Metall. 21 (1973) 1051–1063, https://doi.org/10.1016/0001-6160(73)90021-7.
[17] A.G. Khachaturian, Theory of structural transformations in solids, 1983. https://doi.org/https://www.osti.gov/biblio/5821133.

[18] L.Q. Chen, Phase-field models for microstructure evolution, Annu. Rev. Mater. Sci. 32 (2002) 113–140, https://doi.org/10.1146/annurev.matsci.32.112001.132041.
[19] Z.G. Mei, L. Liang, Y.S. Kim, T. Wiencek, E. O'Hare, A.M. Yacout, G. Hofman, M. Anitescu, Grain growth in U–7Mo alloy: A combined first-principles and phase field study, J. Nucl. Mater. 473 (2016) 300–308, https://doi.org/10.1016/J.JNUCMAT.2016.01.027.
[20] K. Kim, A. Roy, M.P. Gururajan, C. Wolverton, P.W. Voorhees, First-principles/Phase-field modeling of θ′ precipitation in Al-Cu alloys, Acta Mater. 140 (2017) 344–354, https://doi.org/10.1016/J.ACTAMAT.2017.08.046.
[21] N. Saunders, A.P. Miodownik, CALPHAD (calculation of phase diagrams): a comprehensive guide, Elsevier, 1998.
[22] N. Moelans, B. Blanpain, P. Wollants, An introduction to phase-field modeling of microstructure evolution, Calphad 32 (2008) 268–294, https://doi.org/10.1016/J.CALPHAD.2007.11.003.
[23] S. Kovacevic, R. Pan, D.P. Sekulic, S.D. Mesarovic, Interfacial energy as the driving force for diffusion bonding of ceramics, Acta Mater. 186 (2020) 405–414, https://doi.org/10.1016/J.ACTAMAT.2020.01.015.
[24] A.T. Dinsdale, Sgte Data for Pure Elements, Calphad 15 (1991) 317–425.
[25] O. Redlich, A.T. Kister, Algebraic Representation of Thermodynamic Properties and the Classification of Solutions, Ind. Eng. Chem. 40 (1948) 345–348, https://doi.org/10.1021/ie50458a036.
[26] A.J. Ardell, Gradient energy, interfacial energy and interface width, Scr. Mater. 66 (2012) 423–426, https://doi.org/10.1016/j.scriptamat.2011.11.043.
[27] A.A. Mbaye, L.G. Ferreira, A. Zunger, First-Principles Calculation of Semiconductor-Alloy Phase Diagrams, Phys. Rev. Lett. 58 (1987) 49–52, https://doi.org/10.1103/PhysRevLett.58.49.
[28] S.-H. Wei, L.G. Ferreira, J.E. Bernard, A. Zunger, Electronic properties of random alloys: Special quasirandom structures, Phys. Rev. B 42 (1990) 9622–9649, https://doi.org/10.1103/PhysRevB.42.9622.
[29] A. Van De Walle, P. Tiwary, M. De Jong, D.L. Olmsted, M. Asta, A. Dick, D. Shin, Y. Wang, L.Q. Chen, Z.K. Liu, Efficient stochastic generation of special quasirandom structures, Calphad 42 (2013) 13–18, https://doi.org/10.1016/J.CALPHAD.2013.06.006.
[30] A. Van de Walle, M. Asta, G. Ceder, The alloy theoretic automated toolkit: A user guide, Calphad Comput. Coupling Phase Diagrams Thermochem. 26 (2002) 539–553, https://doi.org/10.1016/S0364-5916(02)80006-2.
[31] G. Kresse, D. Joubert, From ultrasoft pseudopotentials to the projector augmented-wave method, Phys. Rev. B 59 (1999) (1999) 1758–1774.
[32] G. Kresse, J. Furthmüller, Efficient iterative schemes for ab initio total-energy calculations using a plane-wave basis set, Phys. Rev. B 54 (1996) 11169–11186, https://doi.org/10.1103/PhysRevB.54.11169.
[33] J.P. Perdew, M. Ernzerhof, K. Burke, [ERRATA] Generalized Gradient Approximation Made Simple, Phys. Rev. Lett. 77 (1996) 3865–3868. http://www.ncbi.nlm.nih.gov/pubmed/22502509.
[34] H.J. Monkhorst, J.D. Pack, Special points for Brillouin-zone integrations, Phys. Rev. B 13 (1976) 5188–5192, https://doi.org/10.1103/PhysRevB.13.5188.
[35] Y. Wang, Z.K. Liu, L.Q. Chen, C. Wolverton, First-principles calculations of β″-Mg5Si6/α-Al interfaces, Acta Mater. 55 (2007) 5934–5947, https://doi.org/10.1016/J.ACTAMAT.2007.06.045.
[36] P.W. Voorhees, W.C. Johnson, The Thermodynamics of Elastically Stressed Crystals, Solid State Phys. – Adv. Res. Appl. 59 (2004) 1–201, https://doi.org/10.1016/S0081-1947(04)80003-1.
[37] C. Jiang, First-principles study of ternary bcc alloys using special quasi-random structures, Acta Mater. 57 (2009) 4716–4726, https://doi.org/10.1016/J.ACTAMAT.2009.06.026.
[38] P.E.A. Turchi, V. Drchal, J. Kudrnovsky, A. Perron, Ab Initio Study of Stability, Local Order, and Phase Diagram For a Series of bcc-based Transition Metal Alloys, J. Phase Equilibria Diffus. 41 (2020) 737–755, https://doi.org/10.1007/s11669-020-00846-w.
[39] V. L, The EMTO-CPA Method, Springer, 2007. https://doi.org/10.1007/978-1-84628-951-4_5.
[40] S. Zheng, S. Wang, First-principles design of refractory high entropy alloy VMoNbTaW, Entropy 20 (2018), https://doi.org/10.3390/e20120965.
[41] M. Meyers, K. Chawla, Mechanical Behavior of Materials (2008).
[42] P. Söderlind, O. Eriksson, J.M. Wills, A.M. Boring, Theory of elastic constants of cubic transition metals and alloys, Phys. Rev. B. 48 (1993) 5844–5851, https://doi.org/10.1103/PhysRevB.48.5844.
[43] S. Mesarovic, S. Forest, H. Zbib, Mesoscale Models: From Micro-Physics to Macro-Interpretation, Springer Cham, 2019. https://doi.org/https://doi.org/10.1007/978-3-319-94186-8.
[44] T.S. Lundy, C.J. McHargue, Diffusion of V48 in Vanadium, Trans. Metall. Soc. AIME. 233 (1965) 243.
[45] K. Maier, H. Mehrer, G. Rein, Self-Diffusion in Molybdenum, Z. Met. 70 (1979) 271–276. https://doi.org/doi:10.1515/ijmr-1979-700412.
[46] D. Gaston, C. Newman, G. Hansen, D. Lebrun-Grandié, MOOSE: A parallel computational framework for coupled systems of nonlinear equations, Nucl. Eng. Des. 239 (2009) 1768–1778, https://doi.org/10.1016/J.NUCENGDES.2009.05.021.
[47] J.W. Cahn, F. Larché, A simple model for coherent equilibrium, Acta Metall. 32 (1984) 1915–1923, https://doi.org/10.1016/0001-6160(84)90173-1.
[48] M.P. Gururajan, T.A. Abinandanan, Phase field study of precipitate rafting under a uniaxial stress, Acta Mater. 55 (2007) 5015–5026, https://doi.org/10.1016/J.ACTAMAT.2007.05.021.
[49] I. Schmidt, D. Gross, Directional coarsening in Ni–base superalloys: analytical results for an elasticity–based model, Proc. R. Soc. London. Ser. A Math. Phys. Eng. Sci. 455 (1999) 3085–3106, https://doi.org/10.1098/rspa.1999.0441.
[50] D. Montes de Oca Zapiain, J.A. Stewart, R. Dingreville, Accelerating phase-field-based microstructure evolution predictions via surrogate models trained by machine learning methods, Npj Comput. Mater. 7 (2021) 3, https://doi.org/10.1038/s41524-020-00471-8.
[51] C. Hu, S. Martin, R. Dingreville, Accelerating phase-field predictions via recurrent neural networks learning the microstructure evolution in latent space, Comput. Methods Appl. Mech. Eng. 397 (2022), 115128, https://doi.org/10.1016/J.CMA.2022.115128.
[52] A.K. Thakur, R.P. Gorrey, V. Jindal, K. Muralidharan, A data-driven approach to approximate the correlation functions in cluster variation method, Model. Simul. Mater. Sci. Eng. 30 (2022), 015001, https://doi.org/10.1088/1361-651X/ac3a16.